Contents lists available at ScienceDirect

Nuclear Instruments and Methods in Physics Research B

Depth profile by Total IBA in perovskite active layers for solar cells

M.A. Barreiros [a,*], L.C. Alves [b], M.J. Brites [a], V. Corregidor [c]

[a] Laboratório Nacional de Energia e Geologia, LEN/UES, Estrada do Paço do Lumiar, 22, 1649-038 Lisboa, Portugal
[b] C2TN, Instituto Superior Técnico, Universidade de Lisboa, E. N.10, 2695-066 Bobadela LRS, Portugal
[c] IPFN, Instituto Superior Técnico, Universidade de Lisboa, E. N.10, 2695-066 Bobadela LRS, Portugal

ARTICLE INFO

ABSTRACT

In recent years the record efficiency of perovskite solar cells (PSCs) has been updated exceeding now 20%. However, it is difficult to make PSCs consistently. Definite correlation has been established between the PSC performance and the perovskite film quality which involves mainly morphology, crystallinity and composition. The manufacturing development of these devices is dependent on the characterisation methodologies, on the availability of suitable and reliable analytical techniques to assess the materials composition and quality and on the relationship of these results with the cell performance. Ion beam analytical (IBA) techniques jointly with a micro-ion beam are powerful tools for materials characterisation and can provide a valuable input for the knowledge of perovskite films.

Perovskite films based on $CH_3NH_3PbI_3$ were prepared (from CH_3NH_3I and PbI_2 precursors) in a planar architecture and in a mesoporous TiO_2 scaffold.

Proton and helium micro-beams at different energies were used in the analysis of PSC active layers, previously characterised by SEM-FEG (Scanning Electron Microscopy with a field emission gun) and XRD (X-ray diffraction). Self-consistent fit of all the obtained PIXE (Particle Induced X-ray Emission) and RBS (Rutherford Backscattering Spectrometry) spectra through Total IBA approach provided depth profiling of perovskite, its precursors and TiO_2 and assess their distribution in the films. PbI_2 presence and location on the active layer may hinder the charge transport and highly affect the cell performance. IBA techniques allowed to identify regions of non-uniform surface coverage and homogeneous areas and it was possible to establish the undesired presence of PbI_2 and its quantitative depth profile in the planar architecture film. In the mesostructured perovskite film it was verified a non-homogeneous distribution with a decreasing of perovskite concentration down to the thin blocking layer. The good agreement between the best fits obtained in a Total IBA approach and the experimental data granted reliability to depth profile results for the studied perovskite films.

© 2017 Elsevier B.V. All rights reserved.

1. Introduction

Over the last few years, the power conversion efficiency of perovskite solar cells (PSCs) has been dramatically increased, making them a competitive source for an efficient use of renewable energy. The first perovskite cells were reported in 2009 [1] and nowadays the best can already convert more than 22% [2] of the sunlight energy into electricity.

Organic-inorganic hybrid compounds as organometal trihalide ($CH_3NH_3PbX_3$, X = I, Br, Cl), with the crystal structure of perovskite, have arisen as a new generation of solution processable, low cost and abundant in nature photovoltaic materials. The interest in these semiconductors and their study have been increasing due to their easy fabrication process and excellent optoelectronic properties, such as strong absorption in the ultraviolet–visible range, small band-gaps, high extinction coefficients, high carrier mobility, bipolar transport and large charge diffusion length [3,4]. Perovskites used as absorbers on mesoporous (mp) metal oxide scaffold and more recently as a solid layer in planar heterojunction (PHJ) architecture, have been resulting as high-performance solar cells, exhibiting impressive open-circuit voltages (V_{OC}) (>1 V), short-circuit photocurrent densities (J_{SC}) (>20 mA/cm^2) and power conversion efficiencies (PCE) (>21%). Despite these remarkable values, highly efficient reproducible PSCs are not easy to obtain even from cells produced in the same batch.

It is now well-known that there is a strong correlation between the perovskite film quality and the device performance. Issues like surface coverage, the pore filling and perovskite film morphology, deserve great attention once it was demonstrated that the reproducible highest performances are attainable with the highest perovskite surface coverages, uniform pore filling and controlled

---

perovskite morphology [5–10]. Solution processed methylammonium lead iodide perovskites ($MAPbI_3$) made by spin-coating the precursor solution of methylammonium iodide (MAI) and lead iodide (PbI_2) result very often in non-continuous and non-uniform perovskite films. In addition, cells made of perovskite films containing MAI and PbI_2 whether due to precursors incomplete reaction or resulting from film degradation caused by humidity, for instance, show low PCE values as consequence of the insulator characteristics of these compounds [11]. Photocurrent densities may be further reduced if PbI_2 is close to the tin oxide (FTO) electrode hindering charge collection at this electrode.

For the continuing development of PSCs, almost all authors agree with the need of further investigations related to film morphology, coverage and uniformity and for that purpose several analytical techniques have been used.

To characterise the PSC material energy-dispersive X-ray (EDX) maps with the elemental distribution in cell cross section and elemental depth profile obtained by X-ray photoelectron spectroscopy (XPS) were reported [5] confirming a rather uniform distribution of the perovskite in mp-TiO_2 on the best performing PSC. In other work [11] secondary ion mass spectrometry (SIMS) was used to obtain the depth elemental composition profile of PSCs revealing a layer structure and a graded composition with increased Pb^{2+} and I^- ions toward the substrate due most likely by non-uniform sputtering of the perovskite layer.

Elemental depth profiles of $MAPbI_3$ films formed on mp-TiO_2 were also reported using time-of-flight-SIMS [12] whose measurements combined with X-ray diffraction (XRD) analyses allowed to detect unreacted PbI_2 precursor in the films.

Based on hard X-ray photoelectron spectroscopy (HAXPES), as surface analytical technique, supported by EDX to perform bulk analysis, Philippe et al. [13] investigated the stability of methylamine lead halide perovskites. The experiments have provided valuable information regarding the similarity of chemical composition and, specifically, the surface composition of the investigated materials, $CH_3NH_3PbI_3$ and $CH_3NH_3PbI_{3-x}Cl_x$.

The novelty of the present work is the application of Ion Beam Analysis (IBA) techniques, using a scanning nuclear microprobe with micro or sub-micrometer MeV ion beam resolution, for surface elemental distribution mapping using PIXE [14] as well as determine layers thickness, uniformity and composition depth profile of a perovskite film combining PIXE and RBS [15] data in a Total IBA approach [16]. The use of IBA techniques jointly with a nuclear microprobe has already shown to provide valuable results in the assessment of dye distribution in dye sensitized solar cells [17] or the characterisation of GaN-based transistors [18]. Furthermore, IBA techniques were used to study Cu(In,Ga)Se$_2$ thin films [19,20], another photovoltaic material, proving the analytical potential and suitability of the Total IBA approach in such a complex multi-layered film with graded composition.

In this work, perovskite films based on $CH_3NH_3PbI_3$ were prepared (from CH_3NH_3I and PbI_2 precursors) in a PJH architecture and in a mp-TiO_2 scaffold. The active layer films were studied concerning crystallinity and morphology by XRD and by Scanning Electron Microscopy (SEM-FEG), respectively.

PIXE and RBS, through Total IBA approach, were used to depth profiling perovskite and precursor materials present in the active layers and evaluate their distribution.

2. Experimental

2.1. Perovskite films preparation

Perovskite precursor solutions were prepared using commercially available compounds: lead iodide (PbI_2, Sigma-Aldrich,

99%), hydriodic acid (HI, Acros, 57 wt.% aqueous) and CH_3NH_2 (40% methanol solution) (TCI). *N,N*-dimethylformamide (DMF) and isopropanol (IPA) were dried and freshly distilled according to standard methods [21]. The CH_3NH_3I perovskite precursor was prepared following a procedure described in literature [22].

The TiO_2 compact and mesoporous layers were prepared using the precursor diisopropoxide bis (acetylacetonate) (TAA, Aldrich, 75% wt% in IPA) and a commercially available TiO_2 paste (Dyesol 18NRT, Dyesol), respectively.

Perovskite films were prepared on substrates with FTO/compact-TiO_2 films (PHJ structure) and FTO/compact TiO_2/mp-TiO_2 films.

A compact TiO_2 layer was deposited by spin-coating a 0.15 M solution TAA in 1-butanol at 2000 rpm for 20 s [23] and the films were annealed for 30 min at 500 °C to obtain FTO/compact TiO_2 substrates.

To prepare FTO/compact TiO_2/mesoporous TiO_2 substrates the compact TiO_2 films were dried at 150 °C for 10 min following the deposition, and a mesoporous TiO_2 layer composed of 20-nm-sized particles was deposited by spin-coating at 5000 rpm for 30 s using a commercial TiO_2 paste (Dyesol 18NRT) diluted in ethanol (2:7, weight ratio). After drying at 150 °C 10 min, the TiO_2 films were gradually heated to 500 °C, baked at this temperature for 30 min and cooled to room temperature [24].

The synthesized CH_3NH_3I (0.159 g) compound was mixed with PbI_2 (0.462 g) in anhydrous *N,N*-dimethylformamide (1 ml) at 75 °C, to produce a clear $CH_3NH_3PbI_3$ solution with concentration of 45 wt%. Perovskite films were prepared by spin coating CH_3NH_3-PbI_3 solution (200 µl) at 4500 rpm for 30 s on substrates preheated at 75 °C, and after six seconds anhydrous chlorobenzene (300 µl) was quickly added. The obtained films were then dried at 100 °C for 10 min.

For each type of films (PHJ architecture and mp-TiO_2 scaffold) a batch of n = 10 samples were prepared and observed by SEM to select those that presented a satisfactory morphology, concerning surface coverage. From these, a PHJ $MAPbI_3$ (sample A) and a mp-TiO_2 $MAPbI_3$ (sample B) films were randomly chosen for analysis. Both samples were cut in two similar pieces, one for SEM characterisation and the other for XRD analysis then followed by IBA measurements.

2.2. Characterisation and analytical techniques

For morphological characterisation, the SEM equipment used was a Philips XL30 FEG (field emission electron source). SEM secondary electron images were obtained at an acceleration voltage of 10 kV. For this study, the samples were not coated with any conductive surface layer.

Active layer compounds were identified by XRD using a Bruker-AXS D8 Discover diffractometer in the θ-2θ configuration. The Cu Kα1 line was collimated with a Göbel mirror and an asymmetric two-bounce Ge (2 2 0) monochromator. The secondary beam passes through an anti-scattering (0.1 mm) slit and it is detected with a scintillation detector. The data were collected with a step size of 0.02°. Crystal structures were identified using Powder diffraction files obtained from the Pearson's Crystal Database (PCD) [25] and Oku [26].

IBA analyses were carried out with an Oxford Microbeams Nuclear Microprobe installed at one of the beam lines of the CTN 2.5 MV Van de Graaff accelerator [27]. Comprising an OM150 quadrupole triplet the experimental setup includes an X-ray and a backscattered particle detection system for PIXE and RBS analysis, respectively. Typical ion beam spatial resolution is of 3×4 µm^2 for a 2 MeV proton beam with ~100 pA beam current.

X-rays are detected with a 30 mm^2 Bruker SDD detector with 145 eV resolution and positioned at 135° with the beam direction

while a 200 mm^2 PIPS detector with 25 keV resolution, positioned at a backward angle of 40° in Cornell geometry, is used for RBS analysis.

2.3. Methodology for spectra analysis

In order to gather sample information over different depths and with different sensitivities, samples were irradiated with proton beams of 2 MeV and 0.9 MeV and He ions with 1.6 MeV. The 2 MeV proton beam allows a good PIXE yield and consequently a fast elemental 2D mapping distribution, that is essential for ascertaining the perovskite film surface homogeneity. From the initial 530 × 530 μm^2 maps recorded, the beam was raster scanned over two apparently homogeneous small sample areas (~50 × 50 μm^2) and PIXE and RBS spectra registered and compared. These two small areas were chosen for establishing both the similarity of

Fig. 1. XRD pattern from PbI$_2$, MAI, together with the patterns obtained from samples A and B.

the two analysed regions (by simple PIXE and RBS spectra comparison) and at the same time define the subsequent analysis area with 1.6 MeV He ions and 0.9 MeV proton beam. The 1.6 MeV He beam was used to gain depth resolution and sensitivity when extracting RBS spectrum information while the analysis with 0.9 MeV proton beam, providing a shallower sample volume analysis than for 2.0 MeV beam, allows increased perovskite X-ray yield relative to X-ray yield of the glass substrate and FTO contact. This provides a better $I_{L\alpha}$ signal due to the smaller interference from Ca K and Sn L lines of the glass substrate and FTO contact, respectively.

All the combined information will allow to achieve a better single solution for the composition and depth profile of the perovskite film.

PIXE spectra were analysed by the GUPIX [28] program in order just to extract the elemental peak areas that were used as PIXE input data for the NDF v9.6a code [29,30] for performing the self-consistent fit of all the RBS and PIXE data obtained for each of the analysed samples.

The X-ray detector efficiency at low and high energies was previously determined by fitting PIXE data obtained under the same experimental conditions of pure binary standards (PbTe, HgTe, Bi$_2$-Te$_3$ and PbI$_2$).

For the RBS fits, the double scattering contribution and the pulse pile-up effect (considering the Molodtsov and Gurbich algorithm [31]) were calculated and the non-Rutherford cross sections for C, N, O and Si were included in the fitting model [32]. The extra contribution to energy spread due to roughness in the perovskite was also considered, being more noticeable when dealing with He beam. The Gamma roughness algorithm was used instead of the Gaussian one, since the obtained values for roughness (σ) are above 20% of the total perovskite layer thickness (t) ($\sigma/t > 0.2$) [33] which, considering the SEM images and the growth method used, can be adequate. Thicknesses are given in at/cm^2 since the exact densities required to calculate real thickness are unknown. Nevertheless, and just for guidance, a rough estimate of those thicknesses is also presented in nm units.
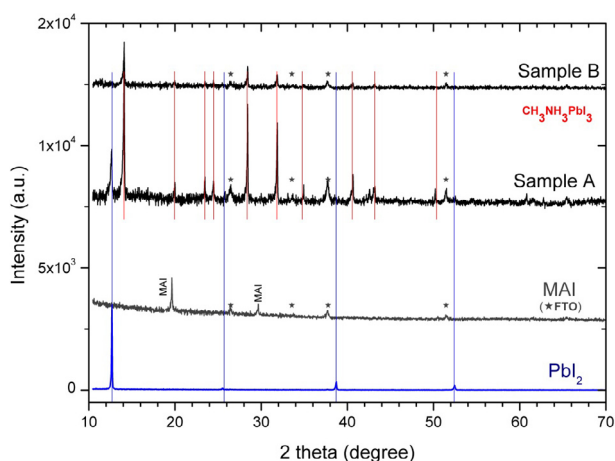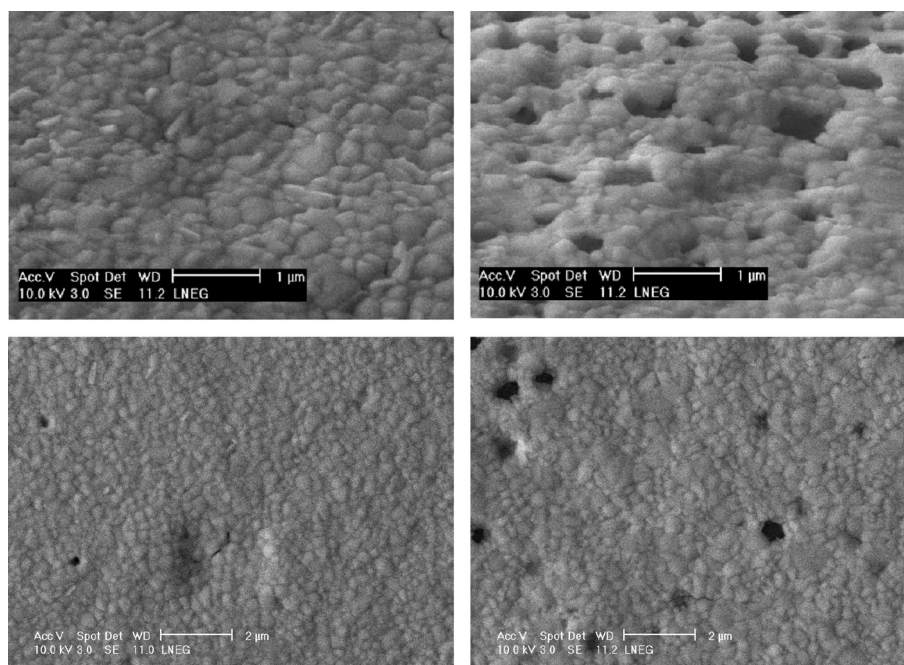
Fig. 2. SEM surface images of samples A (left) and B (right) in front view (bottom row) and tilted (top row).
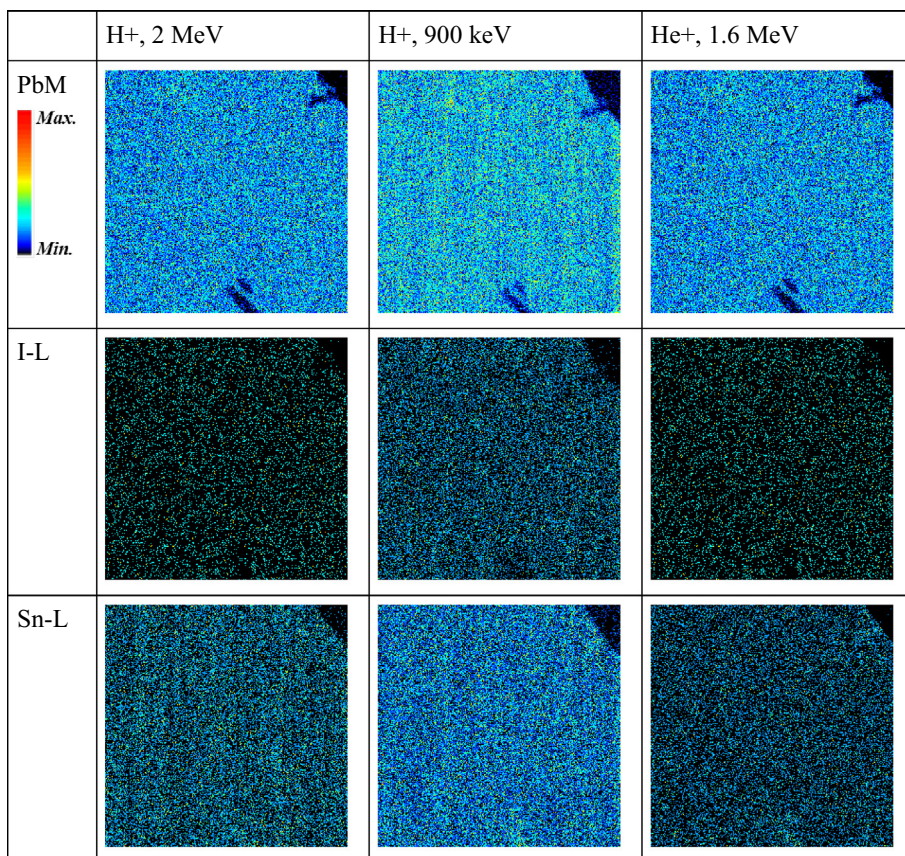
Fig. 3. 2D elemental distribution maps in an area of 530 × 530 μm² for sample A obtained with different type of ion beams (protons and alpha particles) and energies.
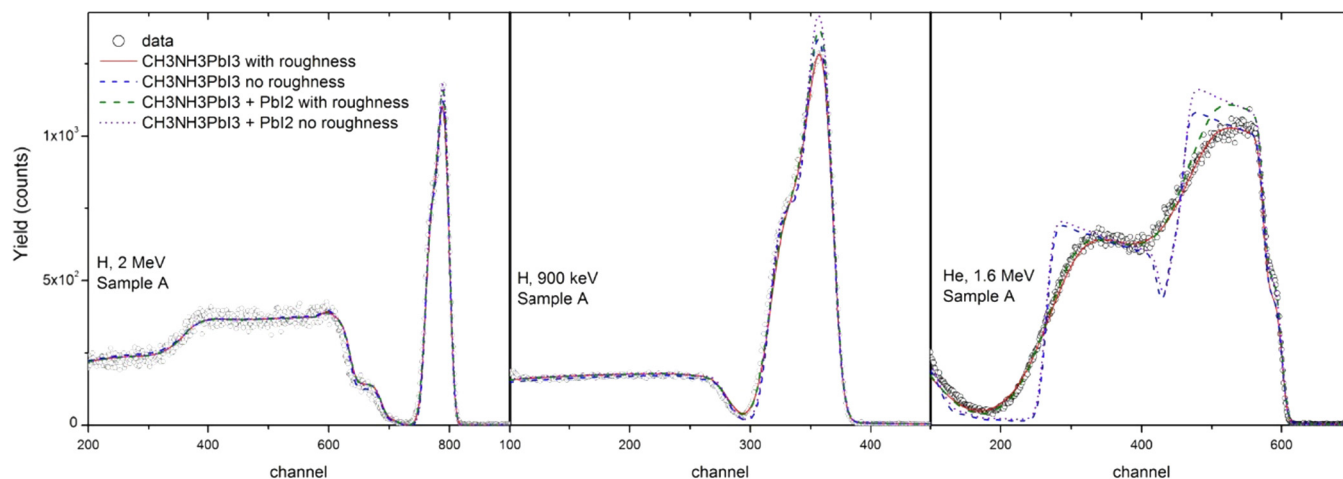
Fig. 4. RBS experimental data and fits (with and without roughness) assuming a pure perovskite layer and a layer containing perovskite and PbI$_2$ (90.1–9.9 at.% respectively).

During the fits, compounds are used instead of single elements assuming a fixed composition for having a more realistic solution, although H atoms cannot be quantified by RBS.

Before proceeding with the series of sequential analysis a random small area of one of the samples was irradiated over 1 h with a 2 MeV proton beam energy and 100 pA beam current and data recorded in a listmode file. The comparison of the spectra obtained at the beginning and at the end of this long run does not reveal any noticeable change then assuring negligible beam irradiation damage.

3. Results and discussion

3.1. XRD analysis

XRD was performed to check the quality of the polycrystalline perovskite film and the presence of unreacted PbI$_2$ and/or MAI precursors. Fig. 1 shows, in bottom panel, the MAI and PbI$_2$ patterns both deposited onto Glass/FTO/TiO$_2$ blocking layer substrates. The top patterns concern sample A and B. For both samples the peaks from MAI are not detectable. Sample A show a rather intense
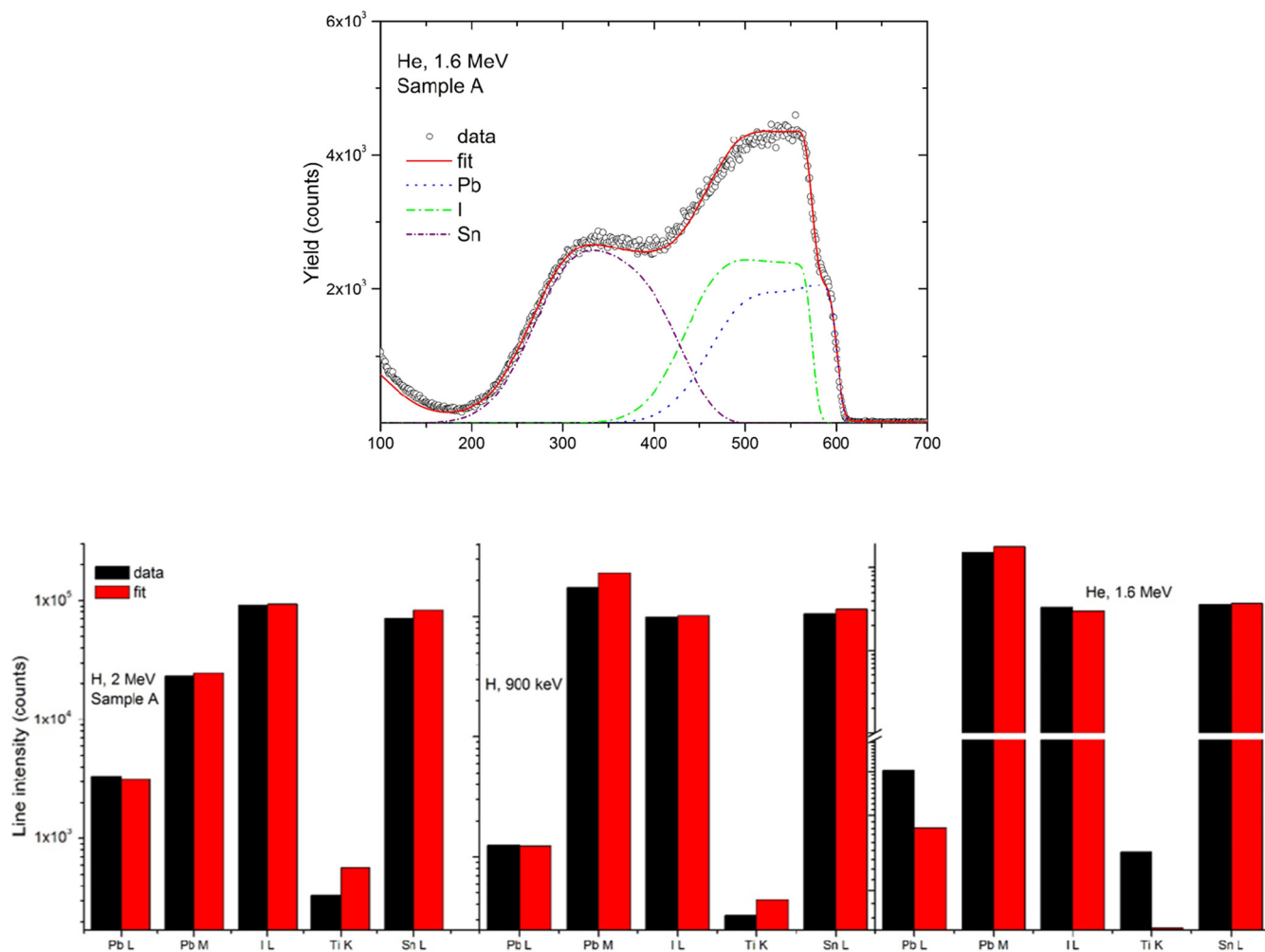
Fig. 5. RBS spectrum and best fit obtained for Sample A, showing the Pb, I and Sn individual contribution. PIXE results (from GUPIXWIN and NDF simulation) for the best found depth profile solution model.

PbI$_2$ main peak (12.7°-(0 0 1) plane). In sample B, no peak from this precursor is observed, confirming the more complete reaction of MAI and PbI$_2$ in a mesoporous scaffold [11]. Nevertheless, both samples exhibit strong peaks located at 14.1°, 28.4° and 31.8°, corresponding to (1 1 0), (2 2 0) and (3 1 0) planes, respectively, of the tetragonal perovskite structure that are in good agreement with literature values [6,26].

3.2. SEM

Fig. 2 presents the SEM images of sample A and B. MAPbI$_3$ crystals exhibit a rather uniform grain morphology and size over the entire sample A surface. Instead, sample B shows a much irregular surface coverage and a rougher surface. However, the grain size and boundaries seem to be similar for samples A and B when compared to the vast diversity of surface morphologies found in literature for MAPbI$_3$ films.

3.3. IBA measurements

3.3.1. Sample A (PHJ MAPbI$_3$)

As can be seen in the 2D maps (Fig. 3), the elemental distribution over the surface presents a quite large homogeneous area, being true for the different layers of the sample (active and conducting layers) since the different beams used can penetrate at different depths. Only small sample areas show evident lack of perovskite film coverage.

Fig. 4 shows the RBS experimental spectra obtained on a small area (50 × 50 μm^2) of the rastered area using the different beams. As it is expected, from the RBS spectrum obtained using the He$^+$ beam (alpha-RBS spectrum) more information can be extracted from the top layers, while from the spectra obtained using protons, we can also obtain information from the substrate. It is also true that the effect of film roughness is more evident, and needed to be accounted for, in the alpha-RBS spectrum at low energy edge of the active layer also contributing to the recorded signal from the FTO layer (although roughness does not apply nor is considered in this layer). In Fig. 4 are also included the best two fits obtained using slightly different depth profiles, without and with roughness. These two fits were obtained assuming two different situations:

a) A single layer of pure perovskite (t = 3105 × 10^{15} at/cm^2) and a roughness value derived was σ = 800 × 10^{15} at/cm^2 (σ/t = 0.26), followed by the TiO$_2$ and the FTO layers. Although the fit is reasonably good it is noticeable that it can be improved once the Pb surface barrier height is slightly underestimated.

b) In order to increase the contribution of Pb to the alpha-RBS spectrum at high channels and also considering the XRD data previously showed, a small amount of PbI$_2$ was

considered in the layer, resulting in a much better fit at these channels for a calculated contribution of 9.9 at.% of PbI_2 in a surface layer with thickness $t = 2681 \times 10^{15}$ at/cm^2 and roughness of $\sigma = 630 \times 10^{15}$ at/cm^2 ($\sigma/t = 0.23$).
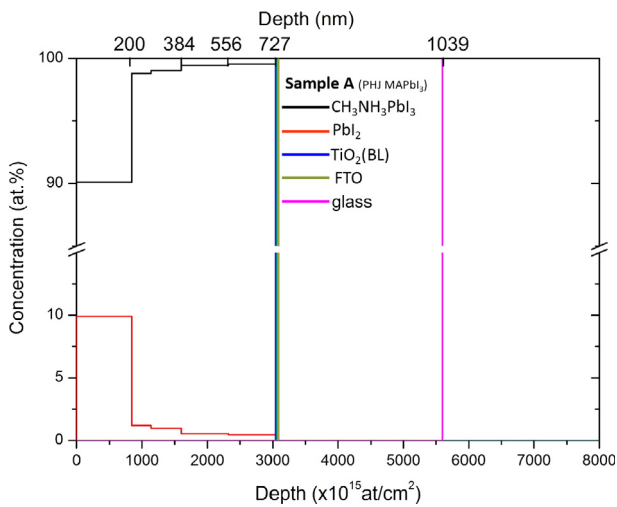
Fig. 6. Compound depth profile obtained for sample A, showing 5 layers with different amounts of perovskite and PbI_2, down to the surface of the very thin TiO_2 blocking layer, followed by the FTO layer (2544×10^{15} at/cm^2) and glass substrate. Values in nm units result from an estimate of the layers density.

As can be seen in this Fig. 4, the PbI_2 concentration along the perovskite layer cannot be constant. In this sense, the best fit for this sample was achieved with the perovskite film subdivided in 5 layers containing different amounts of $MAPbI_3$ and PbI_2. This best fit is shown in Fig. 5 (only the alpha-RBS spectrum is shown), jointly with the PIXE data, where good agreement between fitted and experimental yields were generally found for I, Pb and Sn (from the FTO electrode).

The compound depth profile resulting from the best obtained fit using the Total IBA approach is shown in Fig. 6. Results demonstrate that, whether due to incomplete precursors reaction or film degradation, the PbI_2 concentration increases from the bottom (0.45%) to the top (9.9%) of the perovskite layer. This tendency is similar over the entire surface of the cell active layer where the 2D PIXE elemental distributions maps do not show any heterogeneity, since the RBS spectra recorded in different places of this defined area are almost equal.

3.3.2. Sample B (mp-TiO$_2$ MAPbI$_3$)

Following the same methodology applied for sample A, the sample with TiO_2 scaffold was studied. The RBS spectra and the best obtained fit are shown in Fig. 7, which are characteristic of the overall surface analysed. Similar to what happened for sample A, the 2D-elemental maps are quite homogeneous and are not shown here.
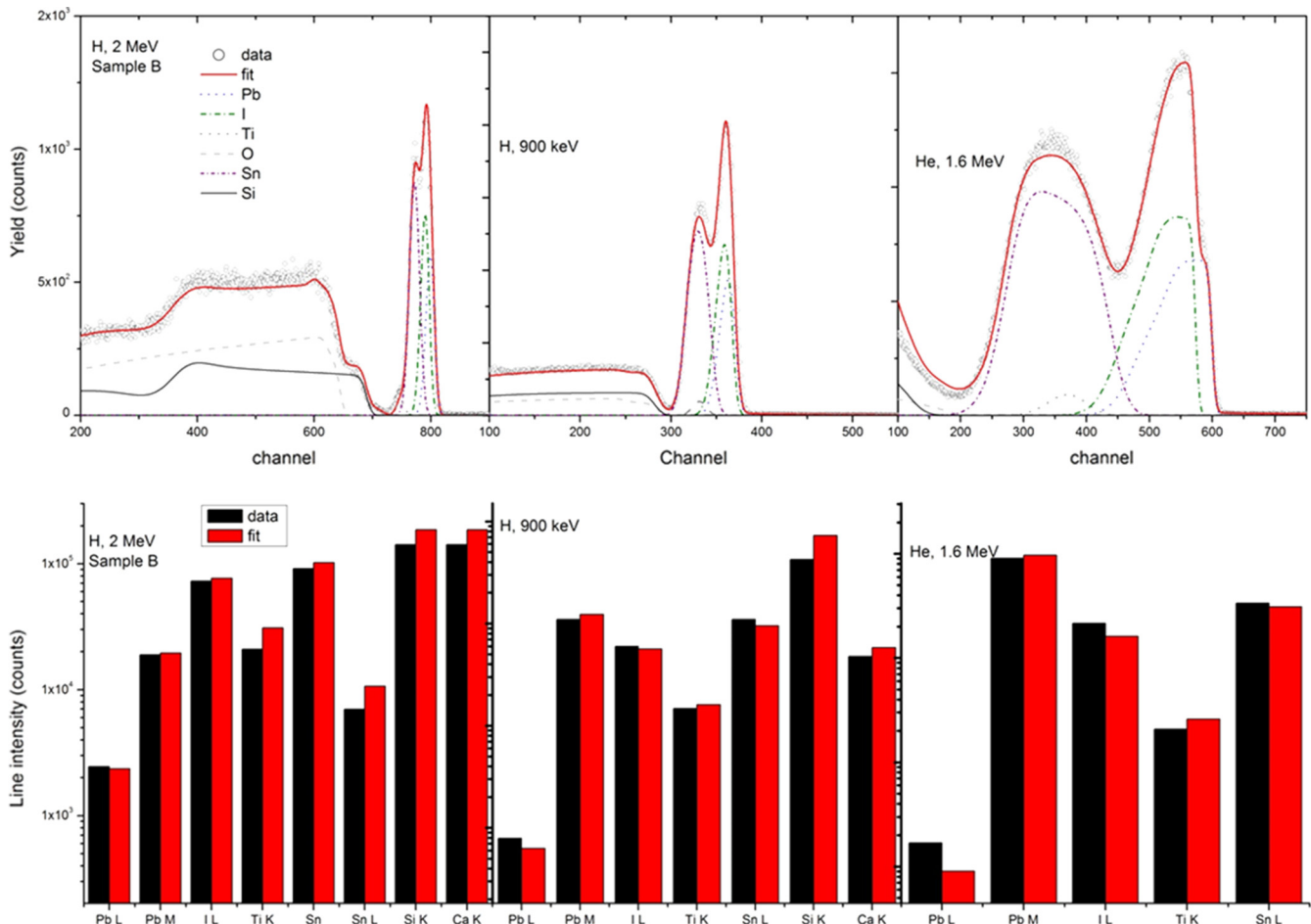
Fig. 7. Best model solution found for Sample B (top row). Experimental data and NDF best fits assuming a pure perovskite layer on top of the sample B film and a concentration gradient of perovskite and TiO_2 scaffold down to the TiO_2 blocking layer. PIXE results (from GUPIXWIN and NDF simulation) for the best found depth profile solution model.
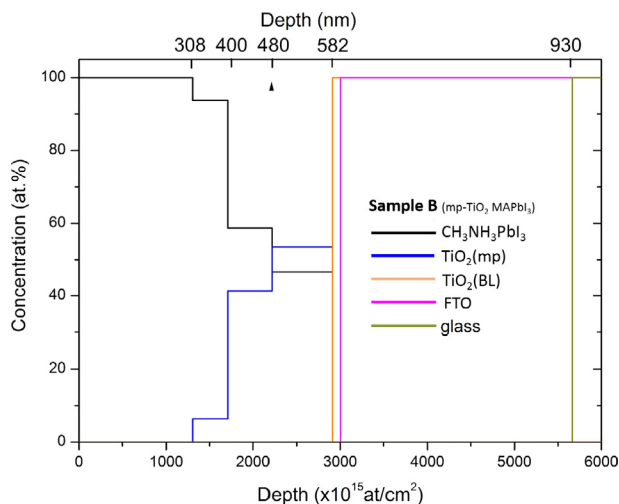
Fig. 8. Depth profile obtained for sample B, showing on top the capping layer followed by 3 layers with different amounts of perovskite and TiO_2 (scaffold), down to the surface of the thin TiO_2 blocking layer (BL), and by the FTO layer and glass substrate.
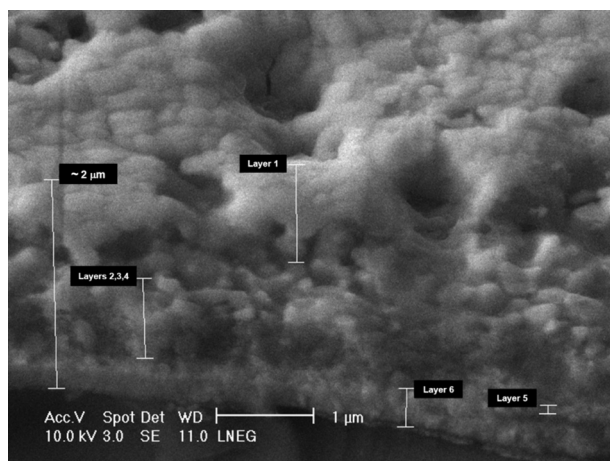
Fig. 9. SEM image of a cross-section of sample B where is possible to identify the physical layers corresponding to the determined depth profile (Fig. 8).

Again deciding to use compounds instead of single elements the best fit was achieved with a profile not containing PbI_2 (Fig. 8) which is in agreement with XRD data. The layers obtained through the model are in agreement with what can be found in the cross-section SEM view presented in Fig. 9, where is clearly noticeable the perovskite capping layer, the mp-TiO_2 plus the $MAPbI_3$ layer (subdivided in 3 layers with different amounts of $MAPbI_3$ and TiO_2), the TiO_2 blocking layer and the FTO electrode. The three layers below the capping layer show inhomogeneous distribution of the perovskite in the mesostructured TiO_2, with a decreasing content of $MAPbI_3$ from 94% to 46%.

4. Conclusions

In recent years, intensive research effort has been made in the development of PSCs to boost the efficiency of these photovoltaics cells. Part of this research is now being applied to the characterisation of the processed materials to produce PSCs.

Based on IBA techniques we have investigated the surface and depth distribution of perovskite ($MAPbI_3$) films and related materials.

These techniques allowed to identify non-uniform surface coverage regions of the perovskite film and helped defining film homogeneous areas.

Considering the PHJ thin film analysis, XRD and IBA both allowed to establish the undesired presence PbI_2 compound, but only IBA was able to ascertain the film surface homogeneity and the quantitative depth profile distribution of PbI_2. For the mesostructured film, other than pure perovskite could not be found (no unreacted precursors nor film degradation), whether in the thin capping layer or in the TiO_2 and $MAIPbI_3$ intermixed layer. It was also verified that a homogeneous TiO_2/perovskite layer does not exist and instead a depth profile concentration down to the thin TiO_2 blocking layer with decreasing perovskite amount was measured.

The results present in this work are a new view on perovskite active layers characterisation once the used methodologies allowed to assess, besides the elemental distribution, the compounds depth profile. The very good agreement between the best fits obtained in a Total IBA approach and the experimental data granted reliability to depth profile results for the studied perovskite films.

Moreover, the implemented methodologies can provide fundamental information to the cell manufacturer once IBA is capable of still giving the same type of information even for a complete cell (including the hole transport material layer and the electrical contact), giving an input to understanding the electrical behaviour of the cell.

The study we presented here pave the way for the characterisation of the recent perovskite films, the mixed-cation lead mixed-halide perovskites for tandem cells [34], an even more challenging system to composition depth profiling.

References

[1] A. Kojima, K. Teshima, Y. Shirai, T. Miyasaka, J. Am. Chem. Soc 131 (2009) 6050–6051.
[2] Best Research-Cell Efficiencies (NREL, 2016); http://www.nrel.gov/ncpv/images/efficiency_chart.jpg.
[3] H. Snaith, J. Phys. Chem. Lett. 4 (2013) 3623–3630.
[4] M. Grätzel, Nat. Mater. 13 (2014) 838–842.
[5] J.H. Heo, S.H. Im, J.H. Noh, T.N. Mandal, C.-S. Lim, J.A. Chang, Y.H. Lee, H. Kim, A. Sarkar, M.K. Nazeeruddin, M. Grätzel, S.Il. Seok, Nat. Photonics 7 (2013) 486–491.
[6] J. Burschka, N. Pellet, S.-J. Moon, R. Humphry-Baker, P. Gao, M.K. Nazeeruddin, M. Grätzel, Nature 499 (2013) 316–320.
[7] G.E. Eperon, V.M. Burlakov, P. Docampo, A. Goriely, H.J. Snaith, Adv. Funct. Mater. 24 (2014) 151–157.
[8] T. Leijtens, B. Lauber, G.E. Eperon, S.D. Stranks, H.J. Snaith, J. Phys. Chem. Lett. 5 (2014) 1096–1102.
[9] D. Bi, A.M. El-Zohry, A. Hagfeldt, G. Boschloo, Appl. Mater. Interfaces 6 (2014) 18751–18757.
[10] J.-H. Im, I.-H. Jang, N. Pellet, M. Grätzel, N.-G. Park, Nat. Nanotechnol. 9 (2014) 927–932.
[11] Z. Xiao, C. Bi, Y. Shao, Q. Dong, Q. Wang, Y. Yuan, C. Wang, Y. Gao, J. Huang, Energy Environ. Sci. 7 (2014) 2619–2623.
[12] H.-S. Ko, J.-W. Lee, N.-G. Park, J. Mater. Chem. A 3 (2015) 8808–8815.
[13] B. Philippe, B.-W. Park, R. Lindblad, J. Oscarsson, S. Ahmadi, E.M.J. Johansson, H. Rensmo, Chem. Mater. 27 (2015) 1720–1731.
[14] Sven A.E. Johansson, John L. Campbell, Klas G. Malmqvist (Eds.), Particle-Induced X-ray Emission Spectrometry (PIXE), John Wiley and Sons Inc, New York, 1995, ISBN 0-471- 58944-6.
[15] Wei-Kan Chu, James W. Mayer, Marc-A. Nicolet (Eds.), Backscattering Spectrometry, Academic Press Inc, San Diego, 1978, ISBN 0-12-173850-7.
[16] C. Jeynes, M.J. Bailey, N.J. Bright, M.E. Christopher, G.W. Grime, B.N. Jones, V.V. Palitsin, R.P. Webb, Nucl. Instr. Method B 271 (2012) 107–118.

[17] M.A. Barreiros, V. Corregidor, L.C. Alves, F. Guimarães, J. Mascarenhas, E. Torres, M.J. Brites, Nucl. Instr. Method B 348 (2015) 255–259.

[18] A. Redondo-Cubero, V. Corregidor, L. Vázquez, L.C. Alves, Nucl. Instr. Method B 348 (2015) 246–250.

[19] A.G. Karydas, I. Bogdanovic Radovic, C. Streeck, C. Kaufmann, R. Caballero, T. Rissom, B. Kanngießer, B. Beckhoff, M. Jaksic, N.P. Barradas, Nucl. Instr. Method B 331 (2014) 93–95.

[20] A.G. Karydas, C. Streeck, I. Bogdanovic Radovic, C. Kaufmann, T. Rissom, B. Beckhoff, M. Jaksic, N.P. Barradas, Appl. Surf. Sci. 356 (2015) 631–638.

[21] D.D. Perrin, W.L.F. Amarego, Purification of Laboratory Chemicals, third ed., Pergamon, Oxford, 1988.

[22] H.-S. Kim, C.-R. Lee, J.-H. Im, K.-B. Lee, T. Moehl, A. Marchioro, S.-J. Moon, R. Humphry-Baker, J.-H. Yum, J.E. Moser, M. Grätzel, N.-G. Park, Sci. Rep. 2 (2012) 591.

[23] J.A. Christians, P.A. Miranda Herrera, P.V. Kamat, J. Am. Chem. Soc. 137 (2015) 1530–1538.

[24] V. D'Innocenzo, G. Grancini, M.J.P. Alcocer, A.R.S. Kandada, S.D. Stranks, M.M. Lee, G. Lanzani, H.J. Snaith, A. Petrozza, Nature 499 (2013) 316–320.

[25] P. Villars, K. Cenzual, Pearsons Crystal Data: Crystal Structure for Inorganic Compounds. Version 1.0, Release 2007/8, ASM International, Materials Park, Ohio, USA, 2007, Powder pattern files.

[26] T. Oku, Crystal Structures of $CH_3NH_3PbI_3$ and Related Perovskite Compounds Used for Solar Cells, Solar Cells – New Approaches and Reviews, L. A. Kosyachenko (Ed.), InTech, doi: 10.5772/59284, 2015.

[27] L.C. Alves, M.B.H. Breese, E. Alves, A. Paúl, M.R. da Silva, M.F. da Silva, J.C. Soares, Nucl. Instrum. Methods B 161–163 (2000) 334–338.

[28] J.L. Campbell, N.I. Boyd, N. Grassi, P. Bonnick, J.A. Maxwell, Nucl. Instrum. Methods B 268 (2010) 3356–3363.

[29] N.P. Barradas, C. Jeynes, R.P. Webb, Appl. Phys. Lett. 71 (1997) 291–293.

[30] M.A. Reis, N.P. Barradas, C. Pascual-Izarra, P.C. Chaves, A.R. Ramos, E. Alves, G. González-Aguilar, M.E.V. Costa, I.M. Miranda, Nucl. Instrum. Methods B 261 (2007) 439–442.

[31] S.L. Molodtsov, A.F. Gurbich, Nucl. Instrum. Methods B 267 (2009) 3484–3487.

[32] A. Gurbich, SigmaCalc 1.6 http://www-nds.iaea.org/sigmacalc/.

[33] N.P. Barradas, E. Alves, S. Pereira, V.V. Shvartsman, A.L. Kholkin, E. Pereira, K.P. O'Donnell, C. Liu, C.J. Deatcher, I.M. Watson, M. Mayer, Nucl. Instrum. Methods B 217 (2004) 479–497.

[34] David P. McMeekin, Golnaz Sadoughi, Waqaas Rehman, Giles E. Eperon, Michael Saliba, Maximilian T. Hörantner, Amir Haghighirad, Nobuya Sakai, Lars Korte, Bernd Rech, Michael B. Johnston, Laura M. Herz, Henry J. Snaith, Science 351 (6269) (2016) 151–155.